Journal of Materials Chemistry C

ROYAL SOCIETY OF CHEMISTRY

PAPER

View Article Online
View Journal | View Issue

Cite this: J. Mater. Chem. C, 2023, 11, 6183

Synthesis of liquid crystals bearing 1,3-dioxane structures and characterization of their ferroelectricity in the nematic phase†

Hiroyuki Matsukizono, [a] Koki Iwamatsu,[b] Sota Endo,[b] Yasushi Okumura,[a] Shizuka Anan [a] and Hirotsugu Kikuchi *[a]

Various structured C3-DIO analogues were synthesized, and their structural and physical properties in liquid crystal phases were investigated through differential scanning calorimetry, polarization optical microscopy, dielectric relaxation, and polarization current measurements. The replacement of fluorine atoms and substitution of other polar functional groups in the C3-DIO structures significantly affected their phase transition behaviour and the emergence of the ferroelectric nematic phase. Among the analogues of C3-DIO, the dipole moments and the generation of the ferroelectric nematic phase were found to be correlated; analogs with vector-added dipole moments below 8.5 D over the whole molecular structure show only the paraelectric nematic phase, whereas those with vector-added dipole moments above 8.5 D over the whole molecular structure show the ferroelectric nematic phase. In particular, the analogue bearing a cyano group gives a large dipole moment of more than 13 D and gives rise to a dielectric constant of more than 14 000 at 100 Hz in its ferroelectric nematic state. The introduction of electron-withdrawing groups at the 4-position of the benzene ring furthest from the dioxane unit in C3-DIO is effective for the enhancement of whole dipole moments and generation of the ferroelectric nematic phase. Our results provide valuable insights into the design of DIO-based molecules with ferroelectric nematic phases.

Received 16th December 2022,
Accepted 3rd April 2023

DOI: 10.1039/d2tc05363b

rsc.li/materials-c

1. Introduction

Liquid crystals (LCs) have been widely used in display technologies,[1,2] electrooptical devices,[1–3] optical modulators,[4,5] and other functional materials[6] because LCs sensitively change their orientation owing to small stimuli such as electric and magnetic fields[1,2] and their interaction with interfaces of substrates.[7] Many molecules exhibit several different types of liquid crystalline properties.[1,2,8,9] In particular, LCs with nematic (N) phases are widely used in practical applications because they respond easily to a small external electric field owing to their high fluidity and long-range correlation length of orientational order.[10,11] In particular, LCs showing blue phases stabilized by polymers, the polymer-stabilized blue phases, exhibit exceptional electrooptical features,[12,13] such as a wide viewing angle, a large Kerr effect,[14,15] and responsivity on the submicron second scale.[12,16] Thus, they could be possible candidates for future LC display materials or fast electro-optical devices. However, these performances require high driving voltages, which prevent their practical use. To reduce the driving voltage, it is effective to apply LC molecules with large dielectric anisotropy.[17]

Ferroelectric materials have attracted significant interest because of their potential for a wide range of applications in capacitors, storage devices, sensors, and optical devices.[18,19] In 2017, we reported that the 1,3-dioxane-based molecule, C3-DIO (**1**), gave a ferroelectric nematic (N_F) phase (referred to as the MP phase in the original paper) with an extraordinarily high dielectric constant of more than 10 000 (Fig. 1).[17] Moreover, Mandle *et al.* reported an unknown N phase of RM734,[20] and its ferroelectric features are confirmed lately.[21] Recently, an LC molecule showing the N_F phase at ambient temperature was also reported by Manabe *et al.*[22] In the ordinary N phase, the dipole moments of LC molecules orient randomly to parallel or antiparallel with respect to the director, resulting in the reduction of macroscopic polarization. In contrast, in the N_F phase, the dipole moments align in the same direction along the director, which integrates the magnitude of the dipole moment to generate macroscopic polarization.[17,21–23] Although

[a] Kyushu University, Institute for Materials Chemistry and Engineering, 6-1 Kasuga-Koen, Kasuga, Fukuoka, 816-8580, Japan. E-mail: kikuchi@cm.kyushu-u.ac.jp
[b] Kyushu University, Interdisciplinary Graduate School of Engineering Sciences, 6-1 Kasuga-Koen, Kasuga, Fukuoka, 816-8580, Japan

† Electronic supplementary information (ESI) available: Experimental details including syntheses, and characterization of C3-DIO analogues: POM images, DSC charts, dielectric relaxation data, switching current response curves and the SHG results (PDF). See DOI: https://doi.org/10.1039/d2tc05363b

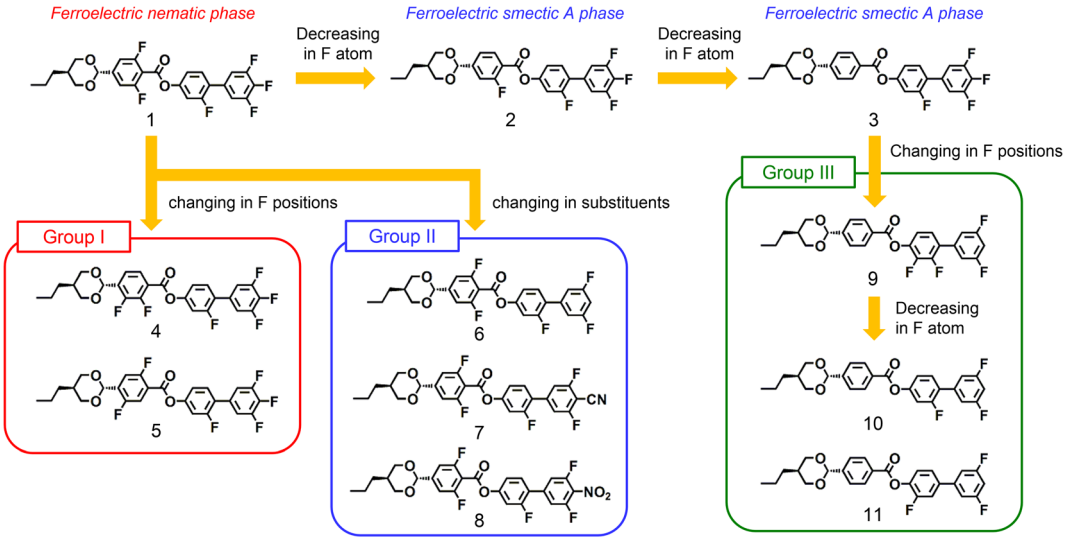

Fig. 1 Chemical structures of C3-DIO (**1**) and its analogues (**2–11**). The newly designed analogues are classified by the modification moieties of the original structure. Group I: analogues modified at their benzoate unit. Group II: analogues modified at their trifluorophenyl unit. Group III: analogues of **3**, which are modified at their phenolate and trifluorophenyl units.

N_F materials have been extensively studied in recent years, the origin of ferroelectricity, including the propagation of the microscopic orientation of molecular dipole moments to macroscopic spontaneous polarization, is poorly understood.

To elucidate the molecular origin of ferroelectricity in detail, it is important to synthesize analogues of LC molecules showing N_F phases, such as C3-DIO and RM734, and evaluate the relationships between their molecular structures and ferroelectric states.[23] It is observed that a decrease in the alkyl chain length of C3-DIO increases the temperature range in which the N_F phase forms. In addition, it has been reported that the temperature required to form the N_F phases of C3-DIO can be changed by mixing it with the geometrical isomer of C3-DIO (*cis*-form).[24] Conversely, there are few reports[23] in which the number and position of fluorine atoms were systematically changed and fluorine atoms were replaced with other functional groups. The reduction of fluorine atoms in C3-DIO generally decreases the dipole moments of the entire molecule, which could impede the emergence of ferroelectric LC phases. However, we observed that C3-DIO analogues composed of non- or 2-fluorinated benzoate units give rise to ferroelectric smectic A (SmA_F) phases instead of N_F phases (Fig. 1).[25] Therefore, it is necessary to evaluate the effect of structural variations on dipole moments, LC phases, and ferroelectricity in detail. Therefore, we synthesized various structured C3-DIO analogues, which are shown in Fig. 1, and analysed their phase transition behaviour, dielectric properties, and ferroelectric features through differential scanning calorimetry (DSC), polarizing optical microscopy (POM), X-ray diffraction (XRD), dielectric relaxation, and polarization reversal current measurements. In addition, we herein discuss their structure–ferroelectric property relationships based on these results and the structural parameters obtained from quantum chemistry calculations.

2. Experimental

2.1. Synthesis of C3-DIO analogues

The synthetic reaction schemes and molecular characterization of compounds **4–11** are described in Section 1 in the ESI.†

2.2. DSC measurement

DSC charts were recorded using a DSC 1 STARe system calorimeter (Mettler Toledo, Switzerland) with a dedicated aluminium pan at a scanning rate of 5 °C min^{-1}.

2.3. POM observation

POM observation was performed using a Nikon ECLIPSE LV100NPOL with a DS-Ri2 camera using four types of cells: no orientation treatment, homogeneous orientation (parallel to the substrate in one direction), planar orientation (parallel to the substrate but with free in-plane orientation), and homeotropic orientation (perpendicular to the substrate). The homogeneous-orientation cells were polyimide-rubbed cells manufactured by E.H.C. The planar orientation cells were prepared by the spin coating method using a toluene solution of poly(methyl methacrylate) (PMMA) on glass substrates and successive drying at 120 °C for 2 h. Homeotropic orientation was performed on a glass substrate by the vapor deposition method using octadecyltrimethoxysilane (180 °C, 2 h, 1 bar).

2.4. XRD measurement

XRD measurements were performed using a Rigaku SmartLab with a Cu Kα (0.154 nm) radiation source (45 kV and 200 mA). The samples were mounted on an Al pan for simultaneous XRD and DSC measurement.

2.4. Dielectric relaxation measurement

Dielectric relaxation spectra were recorded in the range from 1 Hz to 10 MHz using an impedance/gain phase analyser (SI

1260, Solatron Metrology) at an applied voltage of 0.1 V_{rms}. The samples were injected into the homeotropically oriented cells with an electrode area of 1 cm^2 and a cell thickness of 10 μm. The indium tin oxide (ITO) electrode resistance and capacitance were measured using an empty cell, which was used for the correction of the sample impedance to obtain the sample dielectric constants.

2.5. Polarization reversal current measurement and *D–E* hysteresis loop

For polarization reversal current measurements, a waveform generator (2411B, Toyo Technica), an analog-to-digital converter (WaveBook 516A, Toyo Technica), and a current–voltage/charge–voltage (*I–V*/*Q–V*) converter (Model 6254C, Toyo Technica) were constructed. Samples were injected into a homeotropically oriented ITO cell (electrode area = 1 cm^2 and cell thickness = 10 μm) and the polarization reversal current was measured using the triangular wave method. The *D–E* hysteresis loops were obtained by integrating the measured currents. The voltage and frequency ranges of the measurements were −20 to +20 V and 0.1–100 Hz, respectively.

2.6. SHG measurement

SHG measurements were conducted by irradiation with a Q-switched ND:YAG laser (LS-2130, LOTIS TII, Nd:YAG laser wavelength = 1064 nm, energy = 75 μJ, pulse width = 10 ns, pulse period = 20 Hz) to the samples injected in the homeotropically oriented cells (electrode area = 1 cm^2, cell thickness = 10 μm).

2.7. Calculation of dipole moment and structural parameters

The most stable structures and dipole moment (μ) of **1–11** were calculated using DFT with the B3LYP/6-31+G(2d,p) functional implemented using the Gaussian09 program package.[26] From the obtained structures, the dihedral angle (θ) and the angle of the dipole moment with respect to the long axis of the molecules (β) were obtained.

3. Results and discussion

3.1. Molecular design and synthesis of C3-DIO analogues

C3-DIO analogues **4–11** were newly designed based on the C3-DIO structure by changing the positions of fluorine atoms and the types of functional groups to other electron-withdrawing groups, CN or NO_2. These analogues are classified into three groups based on the variation of the three benzene units in C3-DIO. In Group I, the number and substituent position of the F atom were changed in the benzoate unit of C3-DIO (benzene ring adjacent to the dioxane unit). Analogues **4** and **5** are composed of 2,3- and 2,5-difluorinated benzoate structures, respectively. In Group II, the F atom at the 4-position in the 3,4,5-trifluorophenyl unit (benzene ring furthest from the dioxane unit) was changed to another functional group. Analogues **6**, **7**, and **8** were modified with H, CN, and NO_2 groups, respectively. In Group III, the trifluorophenyl and phenolate units (benzene ring second closest to the dioxane unit) of analogue **3** were modified. Compound **9** is an analogue in which the F atom in the trifluorophenyl unit is shifted to the phenolate unit. Compounds **10** and **11** are analogues of **9** and are composed of 3- and 2-fluorinated phenolate units, respectively. These analogues were synthesized by referring to the literature procedures of **1–3**.[17,23,25] The synthetic routes of other analogues are summarized in the ESI.†

3.2. Characterization of C3-DIO analogues in Group I

To evaluate the phase transition behaviour, we performed DSC measurements and POM observations of the C3-DIO analogues in Group I. The results are presented in Fig. S1–S3 (ESI†), and the phase transition temperatures of the analogues are summarized in Table 1. In addition, the dielectric relaxation was measured, and the temperature dependence of the dielectric constant is shown in Fig. S3–S5 (ESI†). These compounds show strong endothermic peaks at approximately 125 °C and weak peaks at 180–200 °C in the 1st heating run. During the cooling process, the peaks appeared in the same temperature range. From POM images, the peaks at 125 °C and 180–200 °C were assigned to the transition of crystalline (Cryst)-N and N-isotropic (Iso) phases, respectively. Thus, the transition from N to other LC phases was not observed. In fact, the dielectric constants of **4** and **5** are *ca.* 10 in their N phases (Fig. S3b, ESI†), which are significantly lower than those in the N_F phase of **1**.

These values slightly decreased at 80–120 °C, which could be caused by phase transition to the Cryst phase. Thus, it is clear that the analogues do not form the N_F phase. These results indicate that the change in substituents at the benzene ring neighbouring the dioxane unit strongly affects the appearance of the N_F phase.

3.3. Characterization of C3-DIO analogues in Group II

The C3-DIO analogues in Group II were investigated for the structural effect of the trifluorophenyl moiety on the emergence of their ferroelectric phase. The results of the thermal analysis, XRD profiles, dielectric relaxation, polarization switching, and second harmonic generation (SHG) measurements for **6–8** are

Table 1 Phase transition behaviour of C3-DIO (**1**) and its analogues (**2–11**) obtained through DSC measurements, POM observation, and the relaxation of their dielectric constants

Group	No.	Phase transition temperature/°C[a]									
	1	Cryst	96[b]	—	—	N_F	69	N_x	85	N	174 Iso
	2		107[b]	SmX_F	85	SmA_F	106		115		207
	3		129[b]	—	—		146	SmA'_F	158		231
I	**4**		125[b]	—	—	—	—	—	—		197
	5		127[b]	—	—	—	—	—	—		180
II	**6**		74[b]	—	—	—	—	—	—		132
	7		121[b]	N'_F	58	N_F	65	N_X	130		244
	8		98[b]		92		96		117		184
III	**9**		128[b]	—	—	—	—	SmX	84		186
	10		124[b]	—	—	—	—		147		185
	11		122[b]	—	—	—	—	—	—		194

[a] Transition temperatures obtained from DSC profiles in the 1st cooling run. [b] Temperatures of the 1st heating run.

shown in Fig. 2 and 3 and Fig. S6–S19 (ESI†). Their phase transition behaviours are summarized in Table 1. Analogue **6** shows a strong endothermal peak at 65 °C and a weak endothermal peak at 132 °C in the 1st heating process, which is assigned to the Cryst-LC and LC-Iso phase transitions, respectively. In the 1st cooling process, these phase transition peaks appeared at 132 and 27 °C with a cooling rate of 1 °C min^{-1}. The POM image of **6** at 130 °C gives a dark-field image and shows bright textures when the temperature decreases below 128 °C, indicating the phase transition from the Iso to N phase. Upon cooling, the colour of the texture continuously changed, and then the textures abruptly changed at 28 °C, which indicates the N-Cryst phase transition.

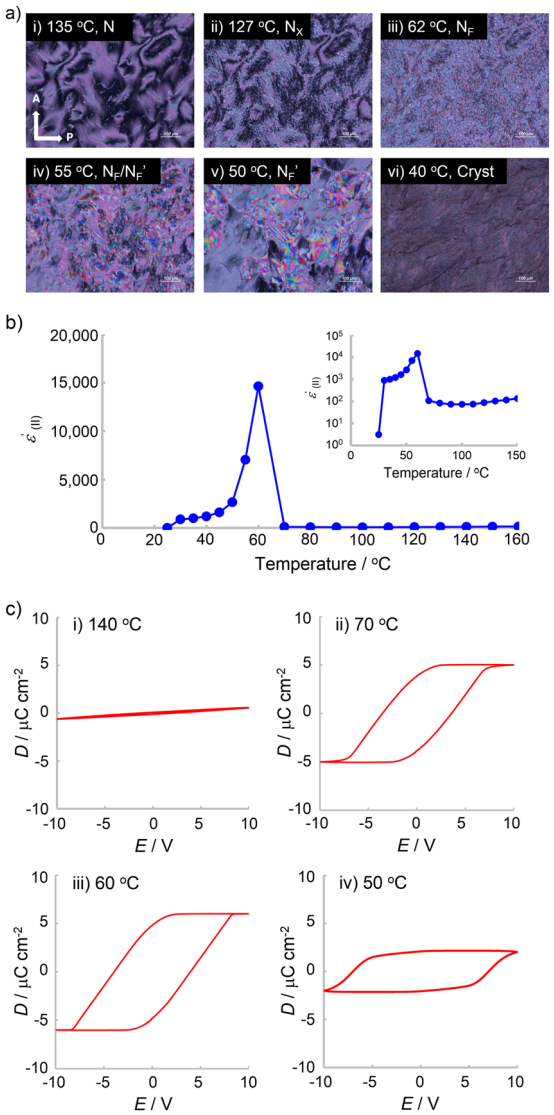

Fig. 2 Characterization of **7** in the cooling process. (a) POM images. The sample was injected into a planar orientation cell. (b) Temperature dependences on the dielectric constant. The sample was injected into a homeotropic orientation cell. F = 100 Hz. 0.1 V_{rms}. (c) Electric displacement—electric field (D–E) hysteresis curves. The sample was injected into a homeotropic orientation cell and the voltage was applied parallel to the director. Voltage: 20 V. Frequency: 200 Hz.

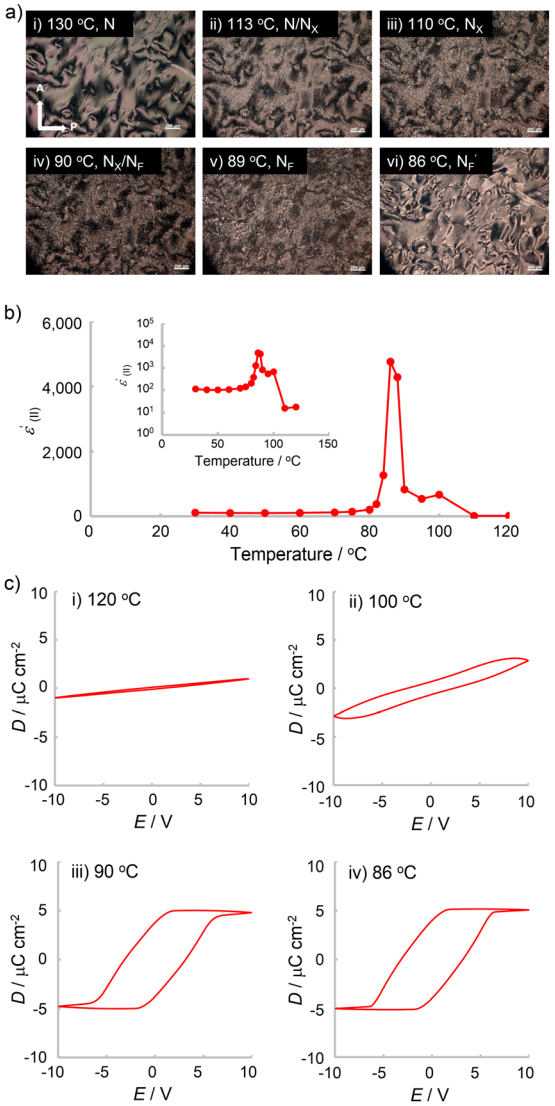

Fig. 3 Characterization of **8** during cooling. (a) POM images. The sample was injected into a planar orientation cell. (b) Temperature dependences of the dielectric constant. The sample was injected into a homeotropic orientation cell. F = 1 kHz. 0.1 V_{rms}. (c) D–E hysteresis curves. The sample was injected into a homeotropic-oriented cell, and the voltage was applied parallel to the director. Voltage: 20 V. Frequency: 200 Hz.

Consequently, a phase transition from N to the other LC phases was not observed. The dielectric constant is *ca.* 10 and almost did not change at 40–120 °C, indicating that **6** only shows the paraelectric N phase.

Analogue **7** showed a strong endothermic peak at 122 °C and a weak peak at 244 °C during the 1st heating process (Fig. S9, ESI†), and these are Cryst-LC and LC-Iso phase transitions, respectively. Conversely, in the 1st cooling process, the peak of Iso-LC phase transition is shown at 244 °C and two weak exothermic peaks newly appeared at 129 and 63 °C. On further cooling, the strong peak appeared at 57 °C, which is attributed to the LC-Cryst transition. However, the weak peak at 58 °C was confirmed before crystallization at a cooling rate of 2 °C min^{-1}, which would be assigned to the transition to another LC phase.

The POM image at 130 °C shows the Schlieren texture characteristic of the N phase (Fig. 2a(i)). At 127 °C, the optical texture changed maintaining their brush-like structures (Fig. 2a(ii)). During further cooling to 62 °C, a region with bright birefringence appeared in the brush areas, and the texture began to flow spontaneously (Fig. 2b(iii)). The observed broken Schlieren texture with fine streak regions is similar to that observed in the N_F phase, which strongly suggests that **7** forms an N_F phase in the temperature range. Actually, **7** gives a huge dielectric constant and a large electric displacement–electric field (*D–E*) hysteresis loop at around 60 °C (*vide infra*). During further cooling, the phase changed to another LC phase (N'_F) at 55 °C (Fig. 2a(iv)), and then Cryst phases formed at 40 °C (Fig. 2a(vi)). The XRD profiles of **7** show a broad peak at 20° characterised by scattering arising from intermolecular spacing in the molecular lateral direction (Fig. S10 and S11, ESI†) at around 150 °C. Although the N–N_X phase transition is observed by DSC and POM results, the peak remained unchanged during cooling to 80 °C, which implies that the order of the N_X phase is as low as that of the N phases. The absence of sharp diffraction peaks in the small-angle region clearly indicates the absence of long-range ordering such as the layer structure, which characterizes the nematic phase.

On further cooling, unfortunately, XRD profiles relating to the N_F and N'_F phases were not observed because of the crystallization of **7**. The temperature dependence of the dielectric constant of **7** is shown in Fig. 2b. The dielectric constant of **7** is *ca.* 100 at 70–240 °C. This value is slightly higher than that of conventional LC molecules, indicating that a weak ferroelectric phase forms partially in this temperature range. When the temperature decreased to 60 °C, the dielectric constant abruptly increased and reached 15 000, clearly indicating the appearance of the N_F phase. On further cooling, the dielectric constant suddenly decreased, whereas the value gradually decreased at 50–30 °C, and the value reached *ca.* 1000 at 30 °C. Considering the POM results, we speculate that the transition from the N_F phase to another type of ferroelectric nematic (N'_F) phase occurred at 50 °C. Below 30 °C, the value suddenly decreased, which could be caused by crystallization. The *D–E* hysteresis curves of **7** are shown in Fig. 2c. At 140 °C, the curve shows a paraelectric aspect (Fig. 2c(i)), which is reasonable because **7** forms the conventional N phase. Upon decreasing the temperature, the *D–E* curve with a large hysteresis was obtained at 70 °C (Fig. 2c(ii)). On further cooling, the curve also showed hysteresis and at 60 °C, the largest hysteresis curve is obtained (Fig. 2c(iii)). The *D* value is *ca.* 6 μC cm^{-2}, which is comparable to that of other reported N_F materials.[17,22,23] Upon further cooling, the *D* value decreased, whereas the hysteresis remained (Fig. 2c(iv)), which also suggests the formation of another N_F (N'_F) phase.

Analogue **8** shows the transition from Cryst to LC phases at 99 °C then transforms into the Iso phase at 185 °C in the heating processes. During cooling, the Iso-LC and LC to other types of LC phase transitions appeared at 184 and 117 °C, respectively. Upon further cooling, two weak peaks appeared at 96 and 92 °C and finally, **8** is crystallized below 37 °C. When the temperature decreased at 5 °C min^{-1}, the weak peaks appeared at 94 and 90 °C, which are slightly lower than those confirmed at a rate of 2 °C min^{-1}. The POM image of **8** at 130 °C shows Schlieren textures characteristic of the N phase (Fig. 3a(i)). During cooling, the textures changed at 113 °C (Fig. 3a(ii)) and the coarse sand-like textures with bright birefringence appeared (Fig. 3a(iii)), which suggests a phase transition to another N (N_X) phase. The phase began to change at 90 °C (Fig. 3a(iv)) and the texture characteristic of the N_F phase appeared (Fig. 3a(v)). Upon further cooling, the texture suddenly changed below 89 °C (Fig. 3a(vi)), which would be assigned to the transition to another N_F (N'_F) phase. The temperature dependence of the XRD profiles of **8** is shown in Fig. S15 and S16 (ESI†). The broad peaks at 20° arising from the intermolecular spacing in the molecular lateral direction slightly shifted to a small angle when the temperature decreased below 110 °C. In addition, a weak peak appeared at 3.5°. This change would be related to the N–N_X phase transition. On further cooling, the peak shifted to a wide angle and its intensity abruptly increased, which suggests that the orders of the N_F and N'_F phases are higher than those of the N and N_X phases. The temperature dependence of the dielectric constant is shown in Fig. 3b. When **8** formed the N phase, the value was *ca.* 10. A gradual increase in the dielectric constant is observed at 90–100 °C. At 88 °C, the value abruptly increased and reached *ca.* 5000. After cooling, the value suddenly decreases and becomes nearly constant below 80 °C. The *D–E* hysteresis curves are shown in Fig. 3c. At 120 °C, **8** gave the N phase and exhibited paraelectric behaviour (Fig. 3c(i)). When the temperature decreased to 90 °C, the curve showed a slight hysteresis loop (Fig. 3c(iii)). At 85 °C, a curve with a large hysteresis was observed (Fig. 3c(iv)). The SHG profiles of **8** are shown in Fig. S19 (ESI†). Although the SHG intensity was quite small at 90–120 °C, it abruptly increased below 90 °C. This means that **8** is SHG active below 90 °C, which is roughly consistent with the results of dielectric relaxation and polarization reversal current measurements. These results clearly indicate the presence of the N_F phase at **8**.

For the analogues in Group II, the substituents significantly affected the emergence of the N_F phases. The introduction of electron-withdrawing groups leads to the generation of N_F phases probably owing to an increase in the molecular dipole moments. During cooling, N_F–N_X phase transition appears at 63 °C for **7** and 85 °C for **8**, respectively, implying that the NO_2 group efficiently makes N_F phases more stable than the CN group. In addition, the melting points of **7** and **8** are 121 and 98 °C, respectively, which implies that **8** sustains potentially N_F at lower temperatures. Conversely, the dielectric constant of **7** reached 14 000 at 100 Hz, which is almost three times larger than the maximum value of **8** (4500 at 1 kHz). Therefore, we conclude that the CN substituent is effective for enhancing the dielectric constants, and the NO_2 substituent is preferential for the stabilization of the N_F phases over wide temperature ranges. In contrast, for RM734 analogues, the modification with CN instead of NO_2 gave no N_F phases.[20] In contrast to the RM734 system, the C3-DIO system is less affected by the

substituent species at the end of the mesogen unit, which is advantageous for tuning the N_F phases. Consequently, by changing the functional group at the 4-position in the phenyl group furthest from the dioxane unit, the emergence of the N_F phase can be controlled. The introduction of electron-withdrawing groups into the position enhances the total dipole moment of the molecule, which could provide preferential effects on the formation of molecular alignment with ferroelectricity.

3.4. Characterization of C3-DIO analogues in Group III

The C3-DIO analogues in Group III were characterized for their thermal and dielectric properties by DSC measurements, POM observations, and dielectric relaxation spectroscopy. The phase transition properties are summarized in Table 1, and the DSC curves, POM observations, dielectric relaxation behaviour, and temperature dependence of the dielectric constant are shown in Fig. S20–S27 (ESI†). The DSC curves of **9–11** show strong endothermic peaks at approximately 125 °C and weak endothermic peaks at 185–195 °C in the 1st heating run (Fig. S20–S22, ESI†), which are assigned to the Cryst-LC and LC-Iso phase transitions, respectively. Although **11** shows only these peaks in the cooling run, **9** and **10** show weak peaks at 84 and 148 °C, respectively. These peaks could be assigned to the transition from LC to other LC phases. The POM images of **9–11** show a dark field image at 182–190 °C and bright textures with birefringence, which are conventional in the N phase at 170–180 °C (Fig. S23, ESI†), indicating that Iso-N phase transitions occur at 185–195 °C. Although **11** shows N-Cryst phase transition at approximately 90 °C, textual changes were observed at 84 °C for **9** and 147 °C for **10** before crystallization. This would be an N–SmX phase transition. The dielectric relaxation of **9–11** was measured at different frequencies, and the temperature dependences of the dielectric constant of **9–11** are plotted (Fig. S24–S27, ESI†). Their dielectric constants were below 40 and were almost constant in the LC phases. The partial decrease in their dielectric constants could be owing to the transition to the Cryst phase. From the results, it is clear that **9–11** did not exhibit N_F phases.

3.5. Quantum chemical calculation of the stabilization structures of C3-DIO analogues

To understand the emergence of the N_F phases, we performed the quantum chemical calculations of C3-DIO analogues and evaluated the relationships between their structural parameters and the emergence of N_F phases. The most stable geometries and dipole moments of these molecules were calculated using density functional theory (DFT) calculation with B3LYP/6-31+G(2d,p) basic functions as previously reported,[26,27] and their structural parameters and dipole moment are summarized in Table 2.

The dihedral angles between the hydrogen atom of the acetal position of the dioxane unit and the adjacent benzene ring, *i.e.*, benzoate structure, were 36.7 and 37.5° for the analogues in group I, which means that the dioxane unit is tilted approximately 53° with respect to the adjacent benzene ring. This is probably due to the steric hindrance arising from the fluorine atom at the 3-position in the benzoate structure. Meanwhile, analogues including those showing ferroelectric phases have dihedral angles of 86.0–89.9°, indicating that the dioxane unit is horizontal to the adjacent benzene ring. Thus, the higher planarity between the dioxane unit and the adjacent benzene ring might be preferable for the expression of the ferroelectric LC phases.

Table 2 Structural parameters and dipole moments obtained using quantum chemistry calculations and the relationships between these parameters and the emergence of ferroelectricity

Group	No.	Dihedral angle/°[a]	μ/D[b]	β/°[c]	μ/D along the molecular axis[d]	Ferroelectric phase[e]
	1	88.9	9.51	9.42	9.38	Y
	2	86.0	9.36	3.99	9.34	Y
	3	89.5	8.69	10.61	8.54	Y
I	**4**	37.5	8.37	7.28	8.31	N
	5	36.7	8.23	13.7	8.13	N
II	**6**	88.9	8.00	11.2	7.84	N
	7	89.0	13.4	6.50	13.3	Y
	8	89.1	13.0	6.66	12.9	Y
III	**9**	89.7	6.86	25.9	6.17	N
	10	89.5	7.18	12.9	7.00	N
	11	89.8	5.92	22.7	5.46	N

[a] Dihedral angle between the H atom of the acetal position in the dioxane unit and the adjacent benzene ring. [b] Denotes the total dipole moments of the entire molecules. [c] Indicates the angles between μ and the long axis of the molecules. [d] Denotes the dipole moments along the long axis of the molecule. [e] Distinction between the emergence of ferroelectric phases. Y and N denote yes and no, respectively. Calculations were performed using density functional theory with the B3LYP/6-31+G(2d,p) basis function. The unit of m is Debye (D), which is defined as a 1×10^{-18} statcoulomb-centimetre.

The total dipole moment and dipole moment along molecular long axes are strongly affected by the number of fluorine atoms and their positions in the molecular structures. The dipole moments of **3**, **6**, and **9**, which have fewer fluorine atoms in their structures, were smaller than that of **1**. In particular, the whole dipole moment of **6** is 8.00, which is significantly smaller than that of the other C3-DIO analogues. This suggests that the substituents at the 4-position in the phenyl unit furthest from the dioxane unit significantly affect the strength of the dipole moment. Conversely, analogues with fluorine atoms positioned against the dipole moments of whole molecules show smaller dipole moments. In particular, the dipole moments of **10** and **11**, which have a hydrogen atom position 4 in the phenyl group furthest from the dioxane unit and fluorine atoms positioned against the whole dipole moments, are significantly small. The dipole moments of analogues forming N_F phases are 8.69–13.4 D, whereas those forming no N_F phases are 5.92–8.37 D in our reports. Thus, a dipole moment of approximately 8.5 D is a boundary for the presence or absence of the N_F phases.

Dipole moments are strongly affected by the changes in molecular conformation. We investigated the effect of the conformation on the value of dipole moments of **3** and **4** showing a dipole moment close to 8.5 D. Analog **3** gives 8.44–9.18 D (Fig. S28, ESI†). In particular, the conformation in which

the COO unit is horizontal with respect to the phenolate structure shows the minimum and maximum values. Meanwhile, **4** shows 8.21–8.75 D (Fig. S29, ESI†). When **4** exhibits a dipole moment above 8.5 D, it adopts the conformation in which the oxygen atoms of the dioxane unit are closer to the fluorine atom of the adjacent benzene ring, which is energetically unstable compared to other conformational changes. These calculation results support that the boundary of the emergence of ferroelectric phases is approximately 8.5 D. However, the analogues of **8** in which the biphenyl mesogen unit is simply converted to 4-nitrophenyl or 3-methoxy-4-nitrophenyl units, and does not exhibit N_F phases despite their dipole moments above 10 D.[23] This implies that the molecular length is also a crucial factor for the emergence of the N_F phases.[23]

Angle β of analogues showing N_F phases is within 4.0–10.6°. Conversely, analogues without ferroelectricity give a β of 7.3–25.9°. Thus, we speculate that the whole dipole moments closer to the dipole moments along the molecular axis are preferential for the emergence of ferroelectricity. From these results, we conclude that the introduction of electron-withdrawing groups at position 4 of the phenyl ring furthest from the dioxane unit is quite effective for designing analogues with N_F phases.

Conclusions

To deeply understand the molecular origin of the ferroelectric nematic phases, we systematically synthesized C3-DIO analogues and investigated their structure–ferroelectric property relationships. In this study, C3-DIO analogues in which fluorine atoms in three species of benzene rings were modified were newly designed and analysed their phase transition behaviour and ferroelectric properties through DSC, POM, dielectric relaxation, and polarization reversal current measurements. The arrangement of fluorine atoms at the benzoate unit strongly affects the formation of N_F phases; non- and 2-fluorinated analogues show ferroelectric smectic phases, whereas 2,3- and 2,5-fluorinated analogues show only paraelectric nematic phases. The arrangement of fluorine atoms in phenolate and 3,4,5-trifluorophenyl units also affects ferroelectricity. The shift of the fluorine atom at the 4-position in the trifluorophenyl unit to other positions led to the disappearance of the N_F phases. Consequently, these arrangements of fluorine atoms decrease the dipole moments of whole molecules, which could be unfavourable for the emergence of ferroelectricity. In contrast, the introduction of electron-withdrawing groups into the 4-position of the 3,4,5-trifluorophenyl unit enhances the dipole moments of the whole molecule and yields N_F phases. In our systems, analogues showing non-ferroelectric N phases give a dipole moment of 5.92–8.37 D, whereas analogues showing N_F phases give a dipole moment of 8.69–13.4 D. Therefore, a dipole moment of around 8.5 D would be a boundary of the emergence of N_F phases in C3-DIO analogues. In addition, we conclude that the introduction of electron-withdrawing groups into the 4-position of the benzene ring furthest from the dioxane unit is effective for the emergence of N_F phases.

Conflicts of interest

There are no conflicts to declare.

Acknowledgements

This work was supported by the Grant-in-Aid for Scientific Research (A) JSPS KAKENHI Grant Number JP18H03920 from the Japan Society for the Promotion of Science (JSPS), the MEXT Project ''Integrated Research Consortium on Chemical Sciences (IRCCS),'' the Dynamic Alliance for Open Innovation Bridging Human, Environment and Materials from the Ministry of Education, Culture, Sports, Science and Technology, Japan (MEXT), and the Cooperative Research Program of ''Network Joint Research Center for Materials and Device''. We would like to thank Editage (**www.editage.com**) for English language editing.

Notes and references

1 H. Bisoyi and Q. Li, *Chem. Rev.*, 2022, **122**, 4887–4926.
2 C. Cuerva, M. Cano and C. Lodeiro, *Chem. Rev.*, 2021, **121**, 12966–13010.
3 M. Gorkunov, I. V. Kasyanova, V. Artemov, A. Ezhov, A. Mamonova, I. Simdyankin and S. Palto, *ACS Appl. Mater. Interfaces*, 2020, **12**, 30815–30823.
4 A. Selmke and F. Cichos, *ACS Nano*, 2014, **8**, 1893–1898.
5 O. Buchnev, N. Podoliak, K. Kaltenecker, M. Walther and V. Fedotov, *ACS Photonics*, 2020, **7**, 3199–3206.
6 Q. He, Z. Wang, Y. Wang, Z. Song and S. Cai, *ACS Appl. Mater. Interfaces*, 2020, **12**, 35464–35474.
7 G. Bryan-Brown, E. Wood and I. Sage, *Nature*, 1999, **399**, 338–340.
8 T. Wöhrle, I. Wurzbach, J. Kirres, A. Kostidou, N. Kapernaum, J. Litterscheidt, J. C. Haenle, P. Staffeld, A. Baro, F. Giesselmann and S. Laschat, *Chem. Rev.*, 2016, **116**, 1139–1241.
9 K. Goossens, K. Lava, C. W. Bielawski and K. Binnemans, *Chem. Rev.*, 2016, **116**, 4643–4807.
10 D.-Y. Kim, S.-A. Lee, D.-G. Kang, M. Park, Y.-J. Choi and K.-U. Jeong, *ACS Appl. Mater. Interfaces*, 2015, **7**, 6195–6204.
11 V. Prasad, S.-W. Kang, K. A. Suresh, L. Joshi, Q. Wang and S. Kumar, *J. Am. Chem. Soc.*, 2005, **127**, 17224–17227.
12 H. Kikuchi, M. Yokota, Y. Hisakado, H. Yang and T. Kajiyama, *Nat. Matter.*, 2002, **1**, 64–68.
13 H. Choi, H. Higuchi, Y. Ogawa and H. Kikuchi, *Appl. Phys. Lett.*, 2012, **101**, 131904.
14 Y. Hisakado, H. Kikuchi, T. Nagamura and T. Kajiyama, *Adv. Mater.*, 2005, **17**, 96–98.
15 Y. Haseba, H. Kikuchi, T. Nagamura and T. Kajiyama, *Adv. Mater.*, 2005, **17**, 2311–2315.
16 Y. Chen, D. Xu, S.-T. Wu, S. Yamamoto and Y. Haseba, *Appl. Phys. Lett.*, 2013, **102**, 141116.
17 H. Nishikawa, K. Shiroshita, H. Higuchi, Y. Okumura, Y. Haseba, S. Yamamoto, K. Sago and H. Kikuchi, *Adv. Mater.*, 2017, **29**, 1702354.
18 S. Horiuchi and Y. Tokura, *Nat. Mater.*, 2008, **7**, 357–366.

19 J. F. Scott, *Science*, 2007, **315**, 954–959.
20 R. Mandle, S. J. Cowling and J. W. Goodby, *Phys. Chem. Chem. Phys.*, 2017, **19**, 11429–11435.
21 X. Chen, E. Korblova, D. Dong, X. Wei, R. Shao, L. Radzinhovsky, M. A. Glaser, J. E. Maclennan, D. Bedrov, D. M. Walba and N. A. Clark, *Proc. Natl. Acad. Sci. U. S. A.*, 2020, **117**, 14021–14631.
22 A. Manabe, M. Bremer and M. Kraska, *Liq. Cryst.*, 2021, 1921867.
23 J. Li, H. Nishikawa, J. Kougo, J. Zhou, S. Dai, W. Tang, X. Zhao, Y. Hisai, M. Huang and S. Aya, *Sci. Adv.*, 2021, **7**, eabf5047.
24 J. Zhou, R. Xia, M. Huang and S. Aya, *J. Mater. Chem. C*, 2022, **10**, 8762–8766.
25 H. Kikuchi, H. Matsukizono, K. Iwamatsu, S. Endo, S. Anan and Y. Okumura, *Adv. Sci.*, 2022, **9**, 2202048.
26 M. J. Frisch, G. W. Trucks,H. B. Schlegel, G. E. Scuseria, M. A. Robb, J. R. Cheeseman, G. Scalmani, V. Barone, G. A. Petersson, H. Nakatsuji, X. Li, M. Caricato, A. Marenich, J. Bloino, B. G. Janesko, R. Gomperts, B. Mennucci, H. P. Hratchian, J. V. Ortiz, A. F. Izmaylov, J. L. Sonnenberg, D. Williams-Young, F. Ding, F. Lipparini, F. Egidi, J. Goings, B. Peng, A. Petrone, T. Henderson, D. Ranasinghe, *et al.*, *Gaussian 09, Revision A.02*, Gaussian, Inc., Wallingford CT, 2016.
27 S.-P. Ju, S. C. Huang, K.-H. Lin, H.-Y. Chen and T.-K. Shen, *J. Phys. Chem. C*, 2016, **120**, 14277–14288.

